Electronic Supplementary Information

Impaired Conjugation Boosts CO_2 Electroreduction by Ni(II) Macrocyclic Catalysts Immobilized on Carbon Nanotubes

Yanjun Huang[a], Hao Dai[b], Dooshaye Moonshiram[c], Zhuofeng Li[d], Zhi-Mei Luo[e], Ji-Hong Zhang[f], Wenxing Yang[d], Yong Shen*[,a], Jia-Wei Wang*[,a,e] and Gangfeng Ouyang*[,a,g,h]

a. KLGHEI of Environment and Energy Chemistry, School of Chemistry, Sun Yat-sen University, Guangzhou 510275, China. Email: cessy@mail.sysu.edu.cn; wangjw25@mail2.sysu.edu.cn; cesoygf@mail.sysu.edu.cn

b. Department of Chemistry, Southern University of Science and Technology, Shenzhen 518055, China

c. Instituto de Ciencia de Materiales de Madrid, Consejo Superior de Investigaciones Científicas (CSIC-ICMM), Sor Juana Inés de la Cruz, 3, Madrid 28049, Spain

d. Center of Artificial Photosynthesis for Solar Fuels and Department of Chemistry, School of Science, Westlake University, Hangzhou, 18 Shilongshan Road, Hangzhou 310024, China.

e. Institute of Chemical Research of Catalonia (ICIQ), Barcelona Institute of Science and Technology (BIST), Avinguda Paisos Catalans 16, Tarragona 43007, Spain.

f. Institutefor New Energy Materials & Low CarbonTechnologies, School of Materials Science and Engineering, Tianjin University of Technology, Tianjin 300384, China.

g. Chemistry College, Center of Advanced Analysis and Gene Sequencing, Zhengzhou University, Zhengzhou 450001, China

h. Guangdong Provincial Key Laboratory of Emergency Test for Dangerous Chemicals, Guangdong Institute of Analysis (China National Analytical Center Guangzhou), Guangzhou 510070, China

Experimental Procedures

X-ray absorption spectroscopy (XAS) methods. The intensity of the X-rays was monitored by three ion chambers (I_0, I_1 and I_2) filled with 70% nitrogen and 30% argon and placed before the sample (I_0) and after the sample (I_1 and I_2). Ni metal was placed between ion chambers I_1 and I_2 and its absorption was recorded with each scan for energy calibration. Ni XAS energy was calibrated by the first maxima in the second derivative of the Nickel´s metal foil's X-ray absorption near edge structure (XANES) spectrum. The samples were kept at 20 K in a He atmosphere at ambient pressure and recorded as fluorescence excitation spectra using a 46-element energy-resolving Ge detector. The complexes were measured in the continuous helium flow cryostat in fluorescence mode. Around 10 XAS spectra of each sample were collected. Care was taken to measure at several sample positions on each sample and no more than 5 scans were taken at each sample position. In order to reduce the risk of sample damage by x-ray radiation, 80% flux was used (beam size 6000 µm (Horizontal) x 1000 µm (Vertical)) and no damage was observed scan after scan to any samples. All samples were also protected from the X-ray beam during spectrometer movements by a shutter synchronized with the scan program. Ni XAS energy was calibrated by the first maxima in the second derivative of the Nickel´s metal X-ray Absorption Near Edge Structure (XANES) spectrum.

Extended X-ray absorption fine structure (EXAFS) analysis. Athena software[1] was used for data processing. The energy scale for each scan was normalized using the Nickel metal standard. Data in energy space were pre-edge corrected, normalized, deglitched (if necessary), and background corrected. The processed data were next converted to the photoelectron wave vector (k) space and weighted by k^2. The electron wave number is defined as $k = \left[2m(E - E_0)/\hbar^2\right]^{1/2}$, E_0 is the energy origin or the threshold energy. K-space data were truncated near the zero crossings k = 2 to 12.352 Å^{-1} in Ni EXAFS before Fourier transformation. The k-space data were transferred into the Artemis Software for curve fitting. In order to fit the data, the Fourier peaks were isolated separately, grouped together, or the entire (unfiltered) spectrum was used. The individual Fourier peaks were isolated by applying a Hanning window to the first and last 15% of the chosen range, leaving the middle 70% untouched. Curve fitting was performed using *ab initio*-calculated phases and amplitudes from the FEFF8[2] program from the University of Washington. *Ab initio*-calculated phases and amplitudes were used in the EXAFS Equation S1.

$$\chi(k) = S_0^2 \sum_j \frac{N_j}{kR_j^2} f_{eff_j}(\pi,k,R_j) e^{-2R_j/\lambda_j(k)} e^{-2\sigma_j^2 k^2} \sin\left(2kR_j + \phi_{ij}(k)\right) \#(S1)$$

where N_j is the number of atoms in the j^{th} shell; R_j the mean distance between the absorbing atom and the atoms in the j^{th} shell; $f_{eff_j}(\pi,k,R_j)$ is the *ab initio* amplitude function for shell j, and the Debye-Waller term $e^{-2\sigma_j^2 k^2}$ accounts for damping due to static and thermal disorder in absorber-back scatterer distances. The mean free path term $e^{-2R_j/\lambda_j(k)}$ reflects losses due to inelastic scattering, where $\lambda_j(k)$, is the electron mean free path. The oscillations in the EXAFS spectrum are reflected in the sinusoidal term $\sin\left(2kR_j + \phi_{ij}(k)\right)$, where $\phi_{ij}(k)$ is the *ab initio* phase function for shell j. This sinusoidal term shows the direct relation between the frequency of the EXAFS oscillations in k-space and the absorber-back scatterer distance. S_0^2 is an amplitude reduction factor.

The EXAFS equation (Equation S1) was used to fit the experimental Fourier isolated data (q-space) as well as unfiltered data (k-space) and Fourier transformed data (R-space) using N, S_0^2, E_0, R, and σ^2 as variable parameters. N refers to the number of coordination atoms surrounding Ni for each shell. The quality of fit was evaluated by R-factor (Equation S2) and the reduced Chi^2 value. R-factor less than 2 % denotes that the fit is good enough whereas R-factor between 2 and 5 % denotes that the fit is correct within a consistently broad model. The reduced Chi^2 value is used to compare fits as more absorber-backscatter shells are included to fit the data. A smaller reduced Chi^2 value implies a better fit. Similar results were obtained from fits done in k, q, and R-spaces.

$$R\text{-}factor = \frac{\sum_i (difference\ between\ data\ and\ fit)^2}{\sum_i (data)^2} \#(S2)$$

Supporting Figures

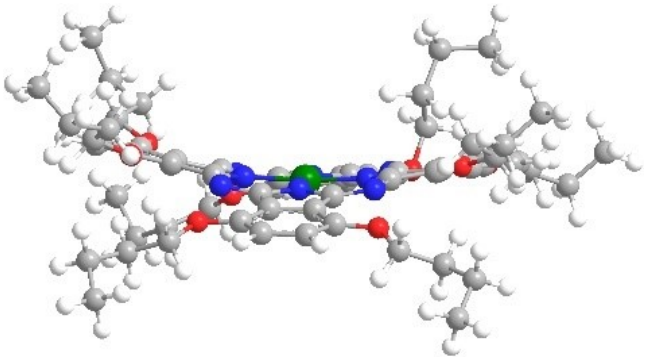

Figure S1. Calculated model of **NiPc-B**.

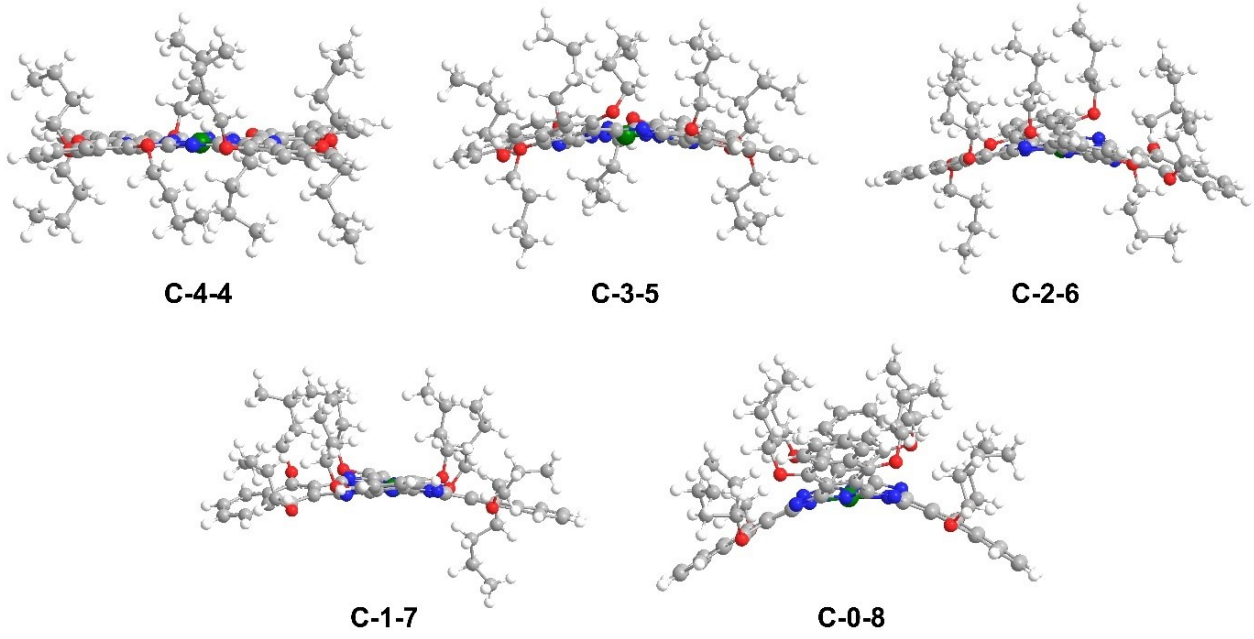

Figure S2. Calculated different conformations of **NiNc-B**.

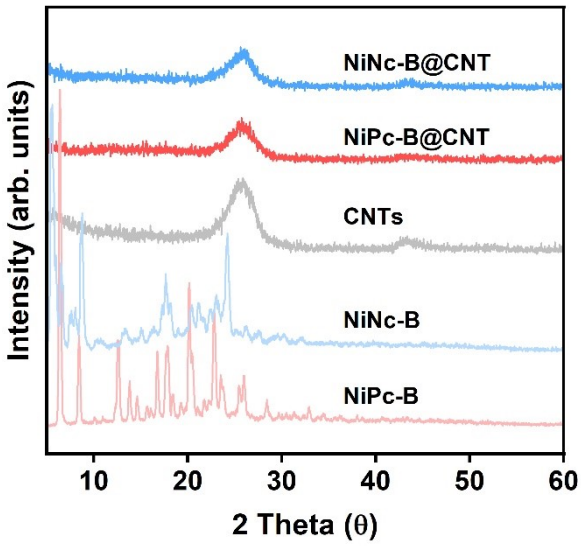

Figure S3. PXRD pattens of **NiPc-B** (red), **NiNc-B** (blue), **NiPc-B@CNT** (pale red), **NiNc-B@CNT** (pale blue) and **CNT** (grey).

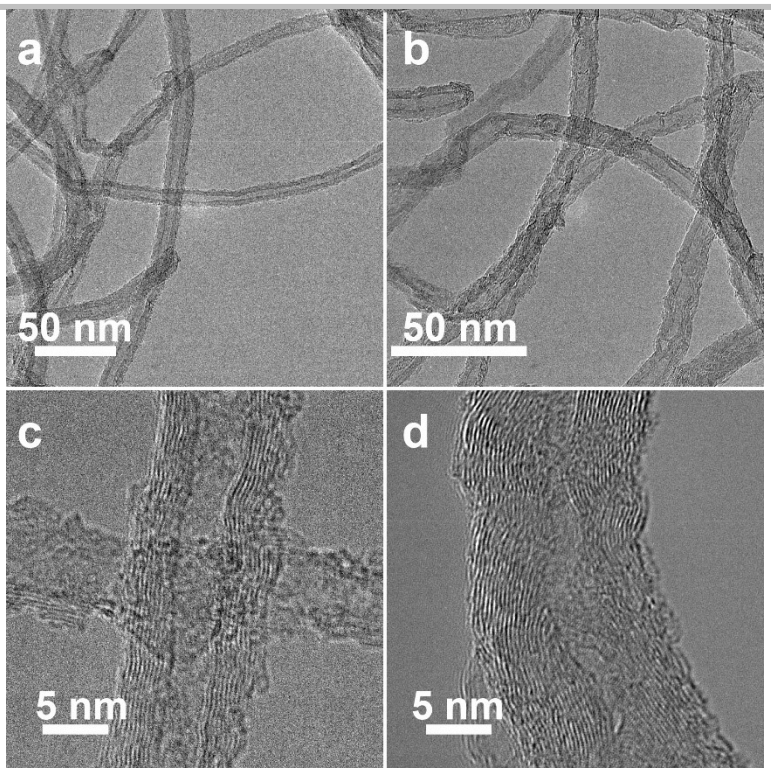

Figure S4. HRTEM images of (a,c) **NiPc-B@CNT** , and (b,d) **NiNc-B@CNT**.

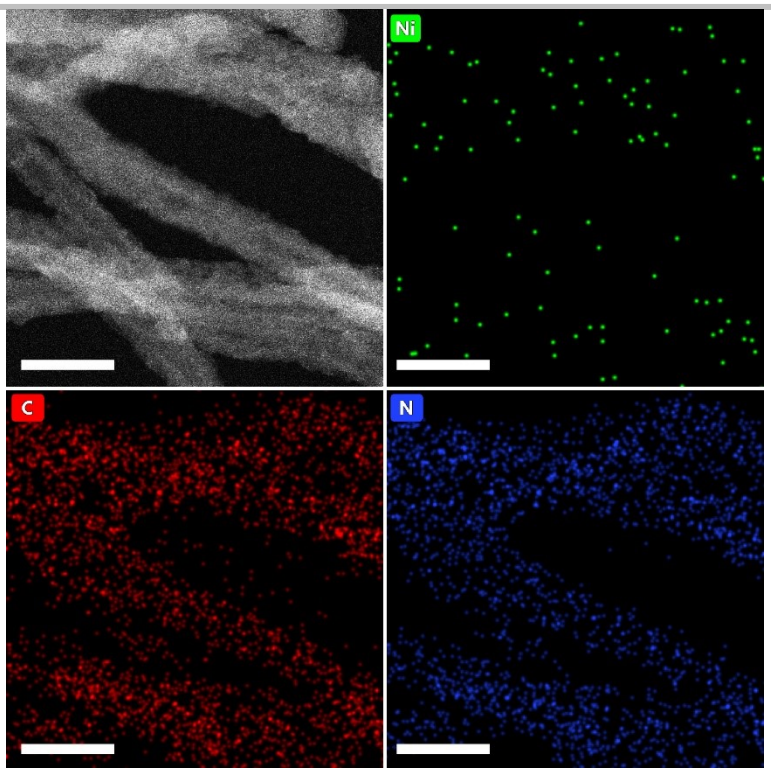

Figure S5. STEM image and EDS elemental mapping of Ni, C, N of **NiPc-B@CNT**. Scale bar: 20 nm.

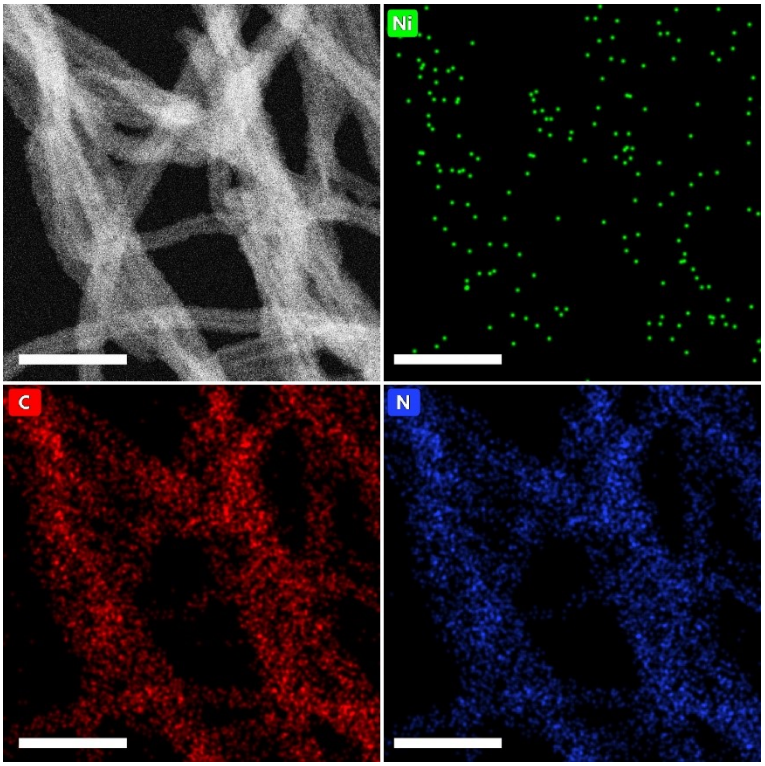

Figure S6. STEM image and EDS elemental mapping of Ni, C, N of **NiNc-B@CNT**. Scale bar: 50 nm.

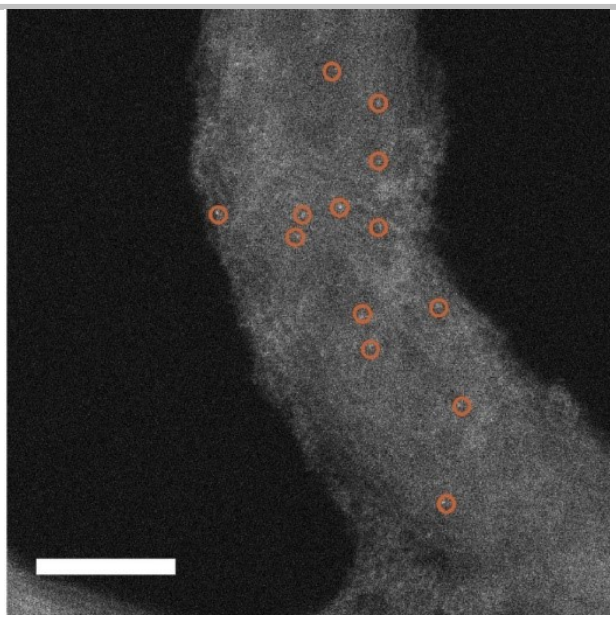

Figure S7. HAADF-STEM images of **NiNc-B@CNT**. Circled bright spots represent dispersed Ni centers. Scale bar: 5 nm.

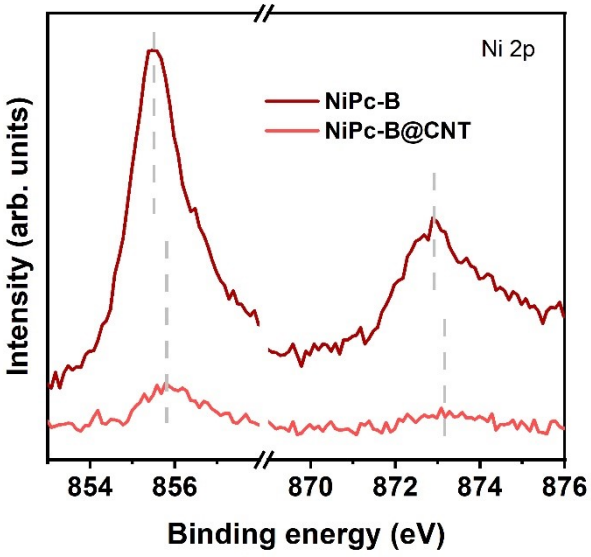

Figure S8. High-resolution Ni 2p XPS spectra of **NiPc-B** and **NiPc-B@CNT**.

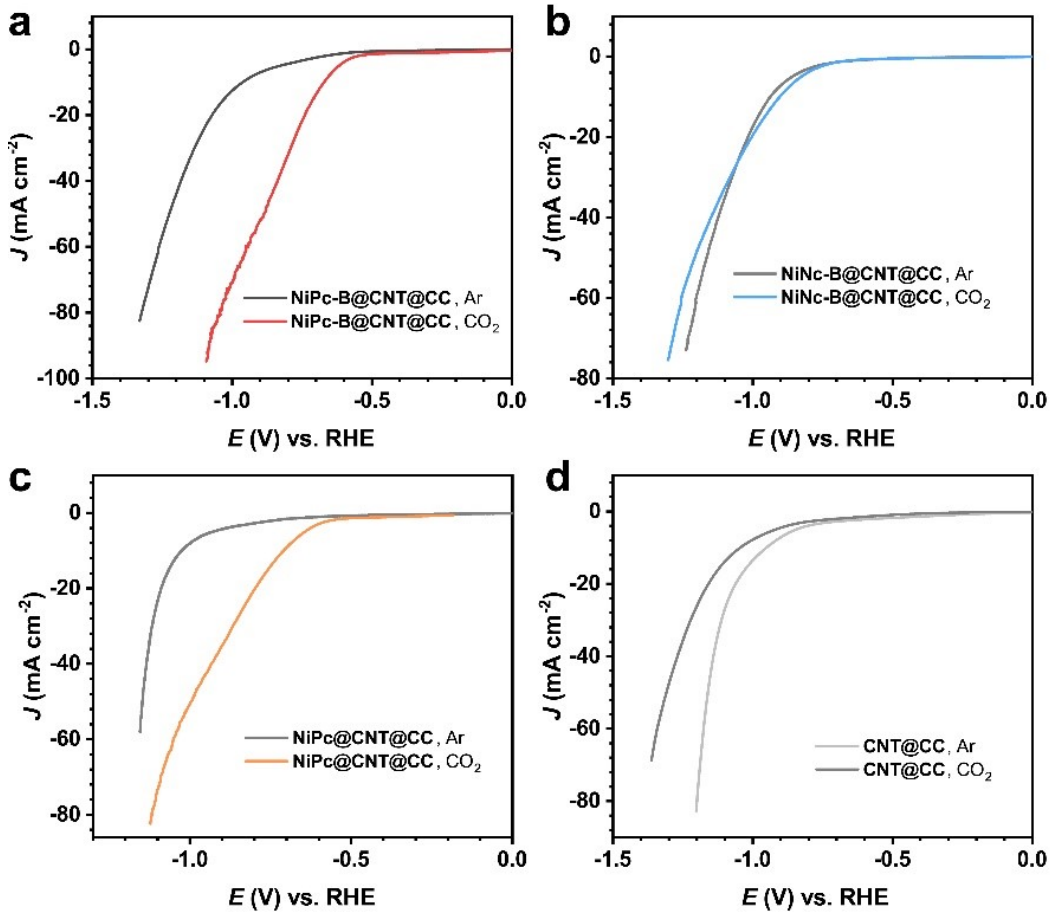

Figure S9. LSV profiles of (a) **NiPc-B@CNT@CC**, (b) **NiNc-B@CNT@CC**, (c) **NiPc@CNT@CC**, and (d) **CNT@CC** in Ar and CO_2 saturated 0.5 M $KHCO_3$ at a scan rate of 10 mV s^{-1} (with *iR* correction).

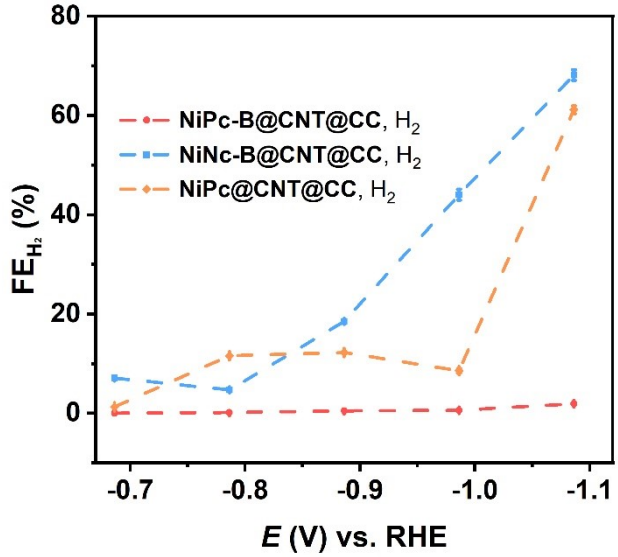

Figure S10. FE_{H2} of **NiPc-B@CNT@CC**, **NiNc-B@CNT@CC** and **NiPc@CNT@CC** at different potentials.

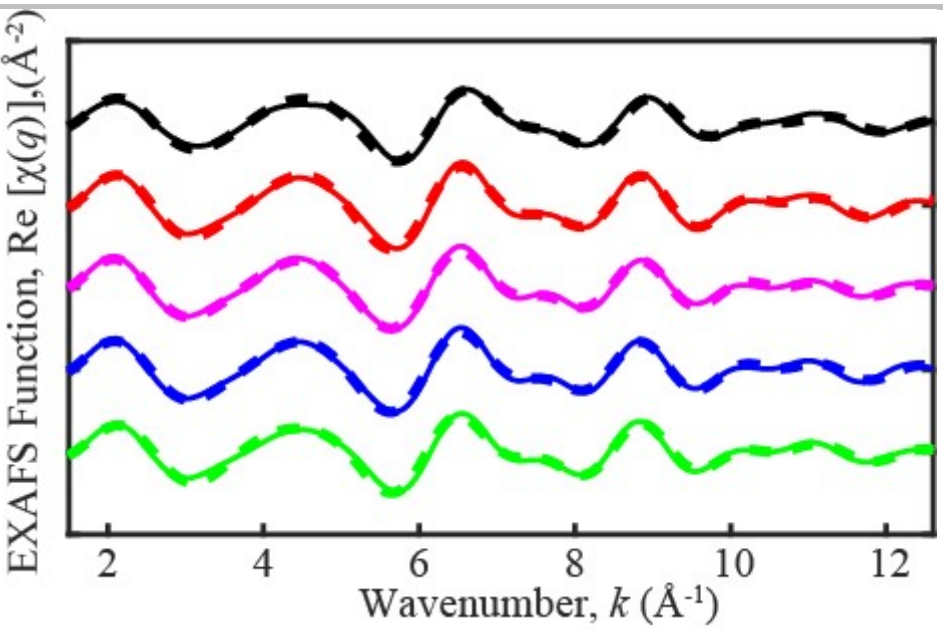

Figure S11. Back Fourier transformed experimental (solid lines) and fitted (dashed lines) *Re*[(χ(*q*)] of **NiNc-B** (green; Fit 3, Table S2), **NiPc-B** (black; Fit 6, Table S2), **NiPc-B@CNT** (red; Fit 9, Table S2), **NiPc-B@CNT@CC** before (magenta; Fit 12, Table S2), and after (blue; Fit 15, Table S2) catalysis.

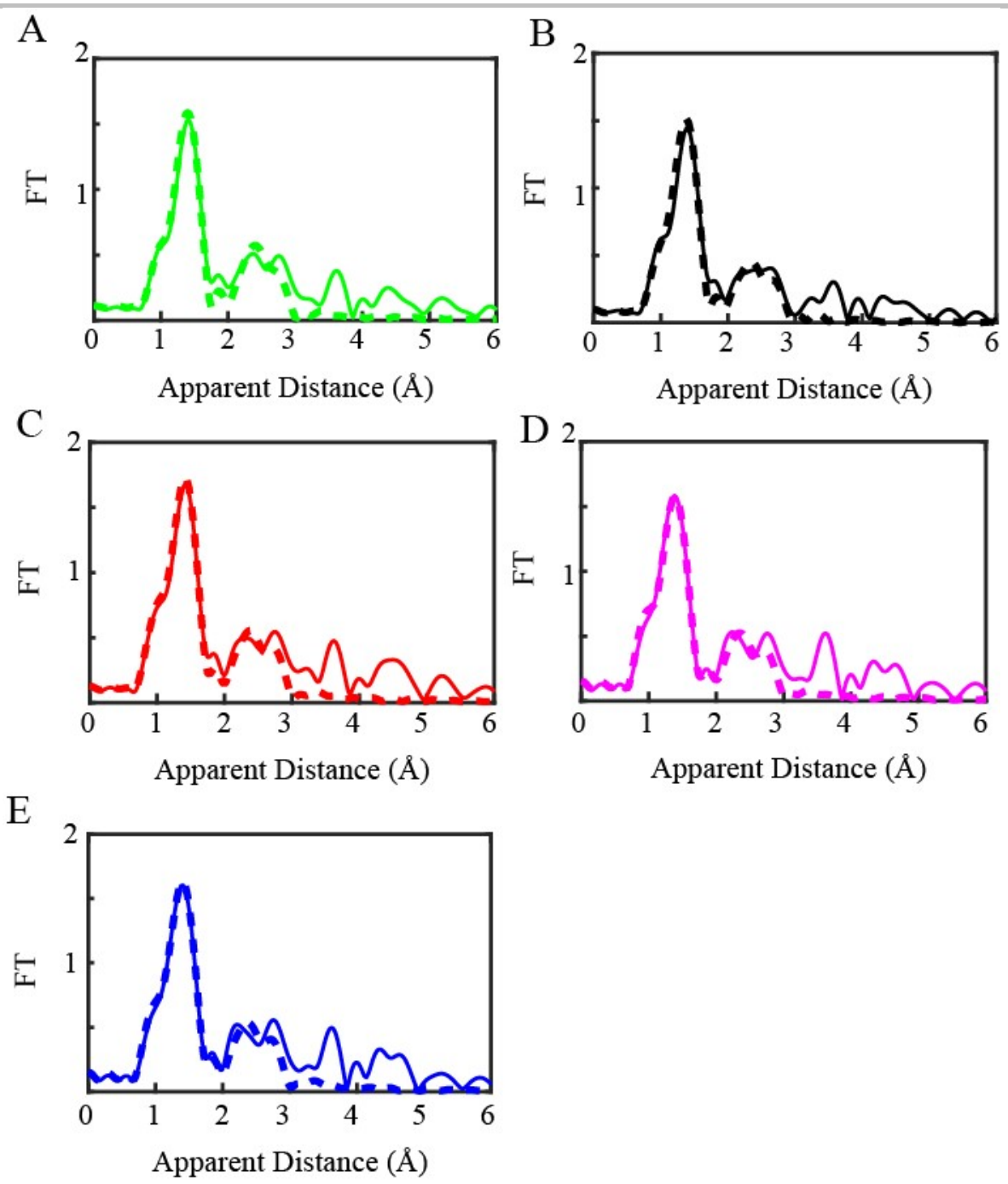

Figure S12. Fourier transforms of experimented (solid lines) and fitted (dashed lines) of k^2-weighted **Ni** EXAFS of (A) **NiNc-B** (green) (Fit 3, Table S2). (B) **NiPc-B** (black) (Fit 6, Table S2). (C) **NiPc-B@CNT** (red) (Fit 9, Table S2). (D) **NiPc-B@CNT@CC** before catalysis (magenta) (Fit 12, Table S2). (E) **NiPc-B@CNT@CC** after catalysis (**blue**) (Fit 15, Table S2).

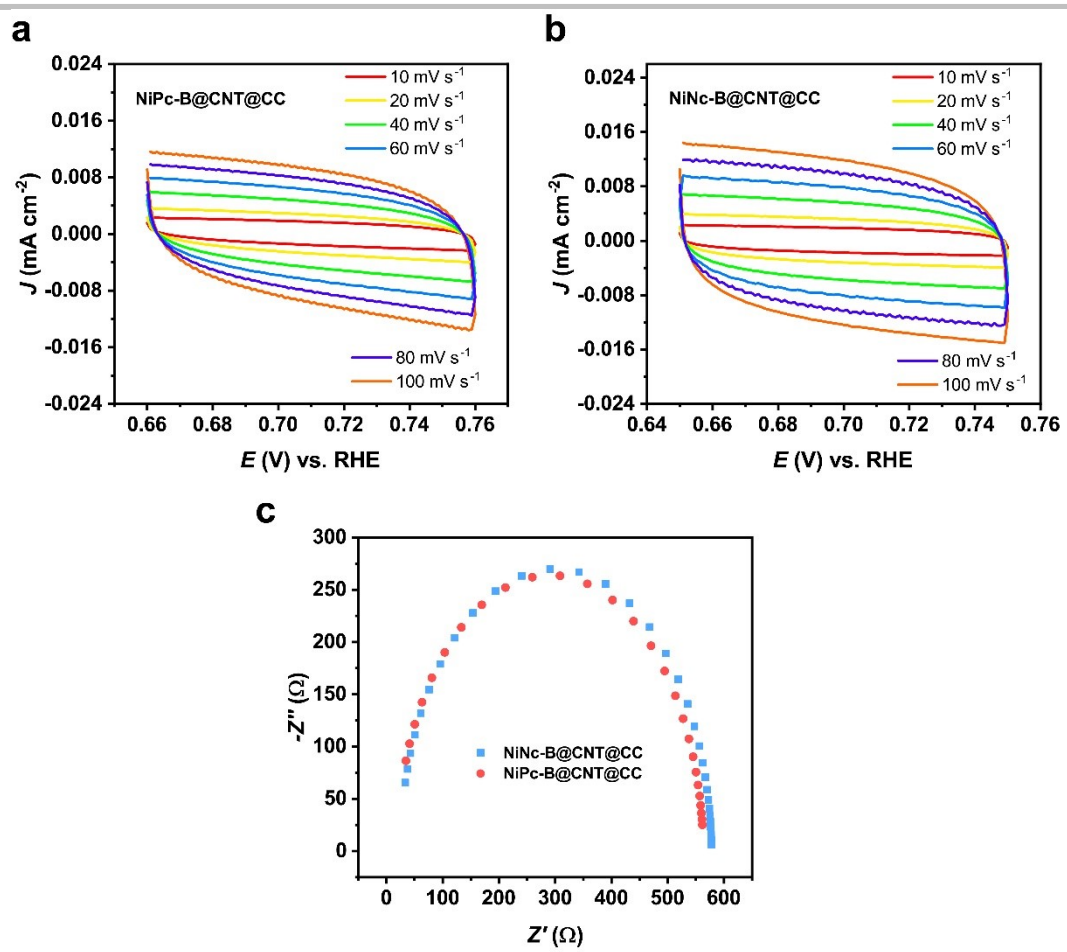

Figure S13. CV scans of (a) **NiPc-B@CNT@CC** or (b) **NiNc-B@CNT@CC** at scan rates of 10, 20, 40, 60, 80, 100 mV s^{-1}. (c) EIS spectra of **NiPc-B@CNT@CC** or **NiNc-B@CNT@CC** at an applied potential of -0.79 V vs. RHE.

.

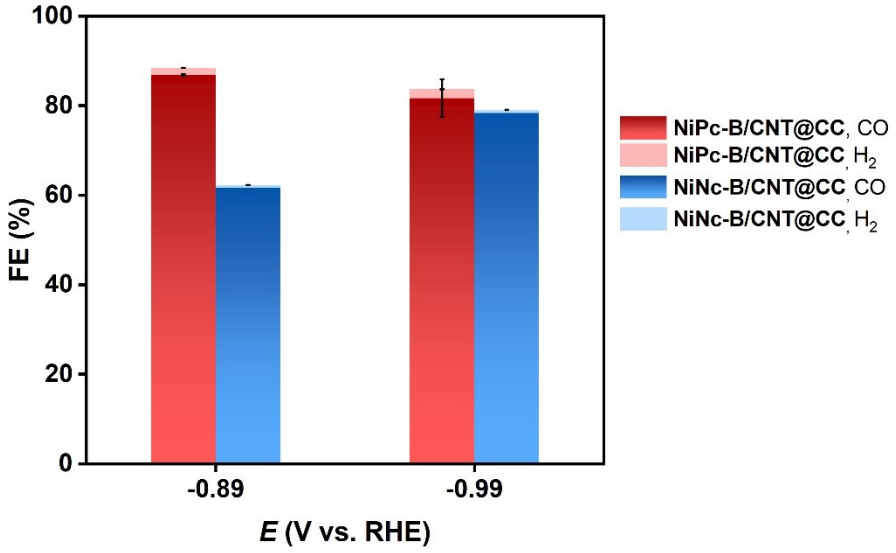

Figure S14. FE_{H2} and FE_{CO} of **NiPc-B/CNT@CC** and **NiNc-B/CNT@CC** at -0.89 and -0.99 V vs. RHE in CO_2 saturated 0.5 M $KHCO_3$ with 30 min of electrolysis.

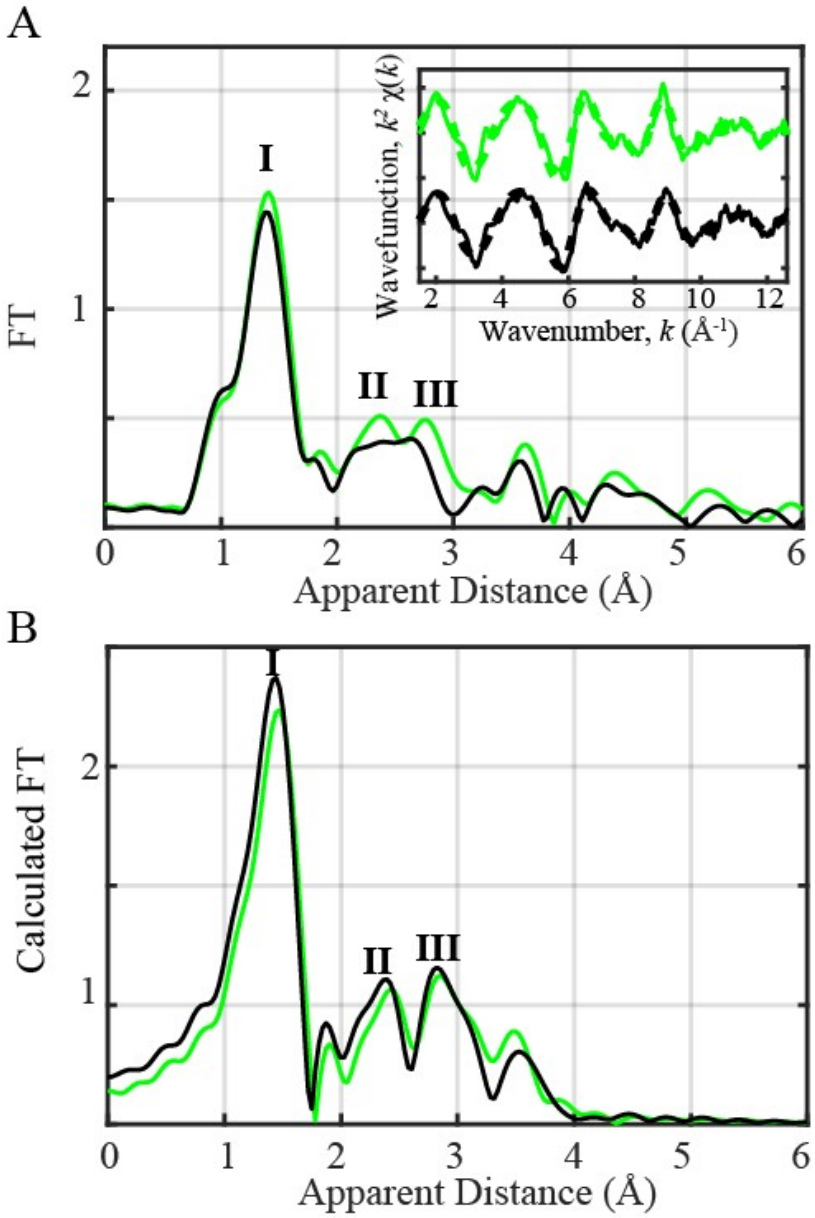

Figure S15. (A) Fourier transforms of k^2-weighted Ni EXAFS of **NiNc-B** (green) and **NiPc-B** (black). Inset: Back Fourier transformed experimental (solid lines) and fitted (dashed lines) k_2[χ(k)] of all Ni complexes. Experimental spectra were calculated for *k* values of 1.5-12.603 Å^{-1}. (B) Simulated EXAFS Spectra **of NiNc-B** (green) and **NiPc-B** (black). Atomic coordinates were obtained from DFT optimized structures.

Analysis of the EXAFS spectra of **NiNc-B** and **NiPc-B** reveals that the averaged Ni-N distances of 1.89 ± 0.01 Å and 1.87 ± 0.01 Å in close agreement with the DFT optimized coordinates, respectively (Table S2), showing that the geometrical theoretical optimizations can be reliably used for understanding the structural conformations of the Ni-based solid and anchored complexes.

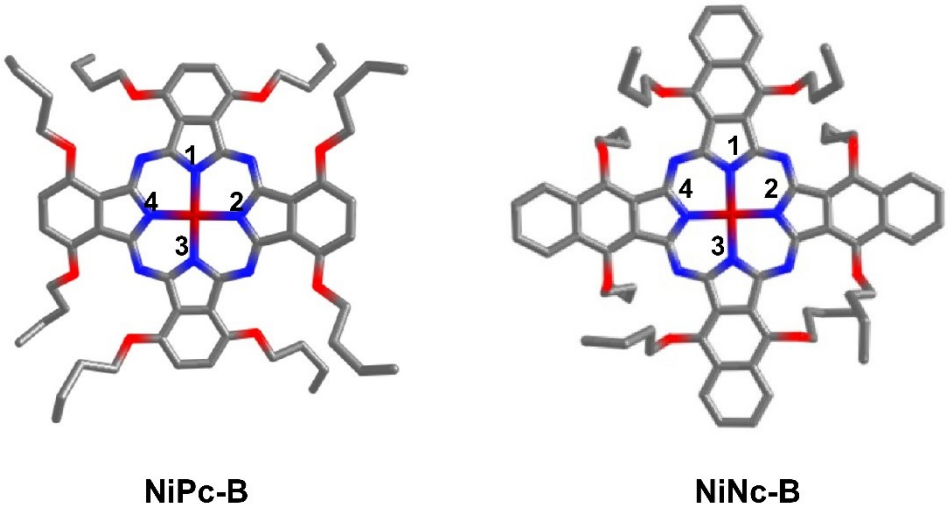

Figure S16. A schematic marking out the number of N atom in **NiPc-B** or **NiNc-B** analyzed by EXAFS.

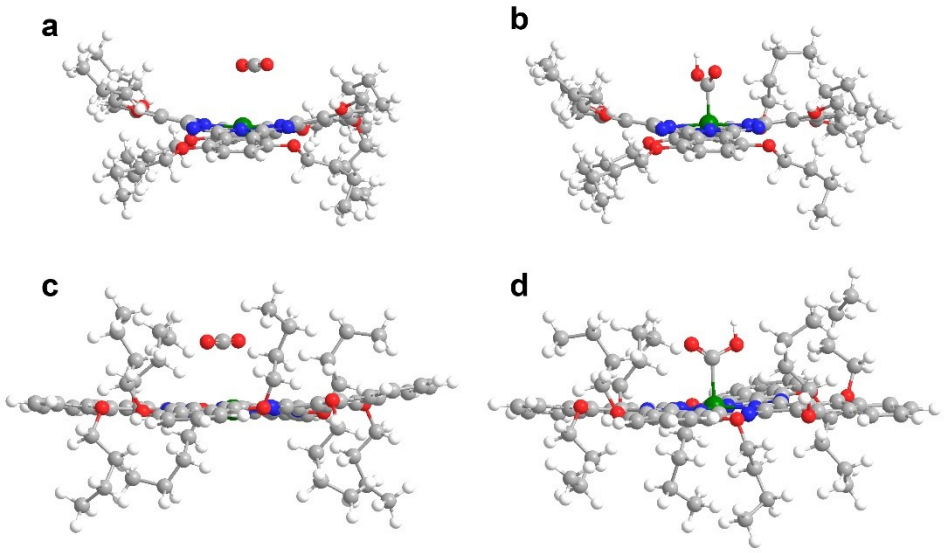

Figure S17. CO_2 adsorption configurations of (a) **NiPc-B** and (c) **NiNc-B**. The optimized structural models of *COOH at the Ni site of (b) **NiPc-B** or (d) **NiNc-B.**

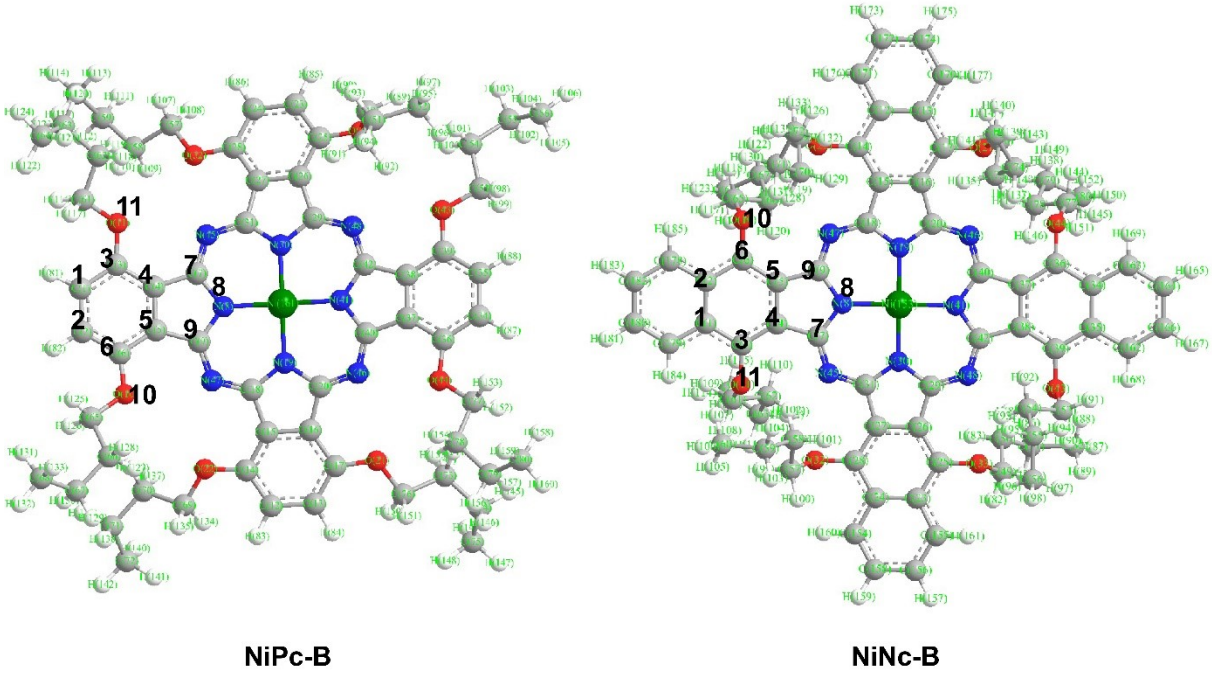

Figure S18. A schematic labelling the atoms of **NiPc-B** or **NiNc-B** analyzed by NPA.

It should be noted that the structures of **NiNc-B** and **NiPc-B** are in symmetry, so only the charges of Ni and atoms 1-11 (the labelled indole ring) were highlighted. The charges of Ni and the sum of charges of atom 1-9 of **NiPc-B** show more negative charges than those of **NiNc-B** (Table S4), respectively, which indicates that the extended benzene ring of **NiNc-B** shows an electron-withdrawing effect on the Ni-indole fragment.

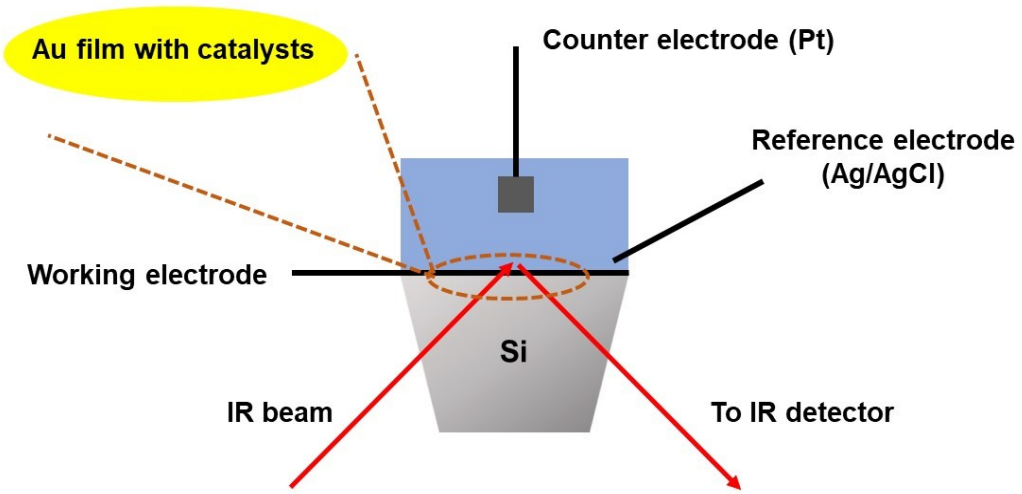

Figure S19. Schematic illustration of three-electrode ATR-SEIRAS configurations.

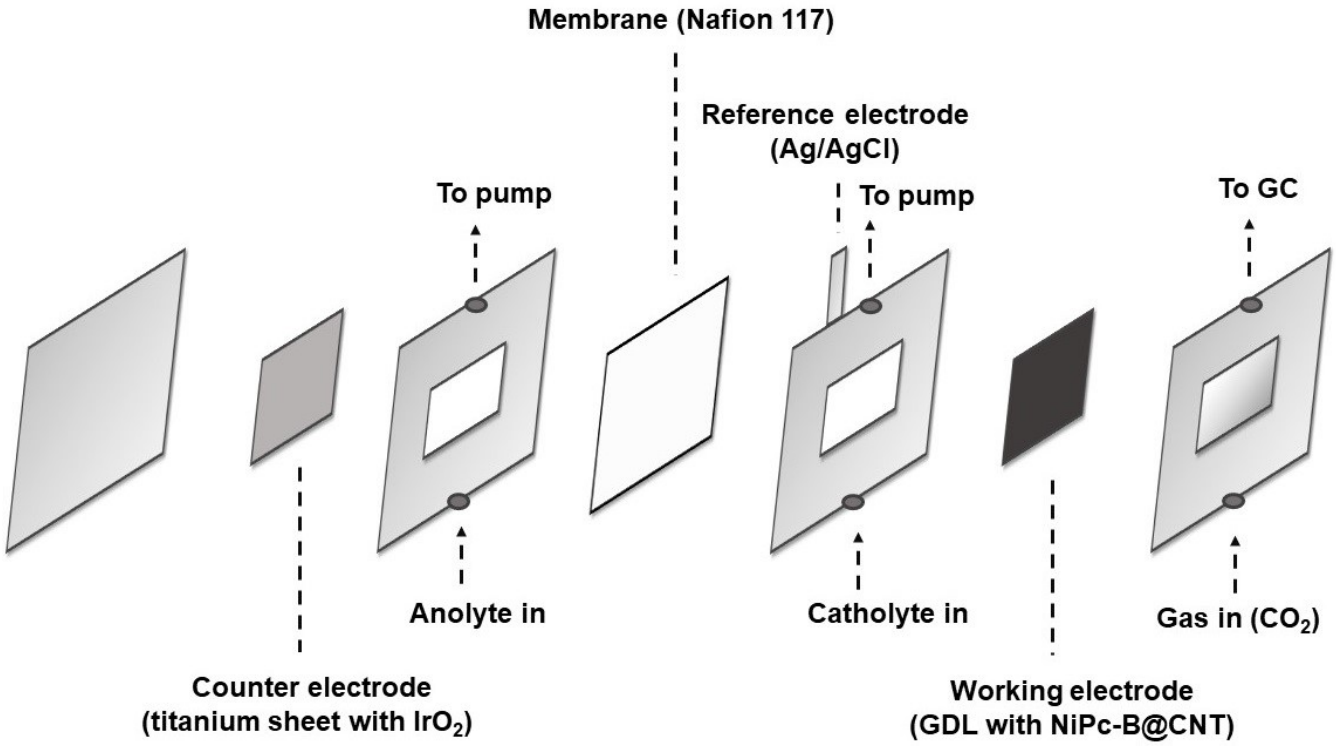

Figure S20. Schematic illustration of three-electrode electrochemical configurations with GDE for CO_2RR. GDL = gas-diffusion layer.

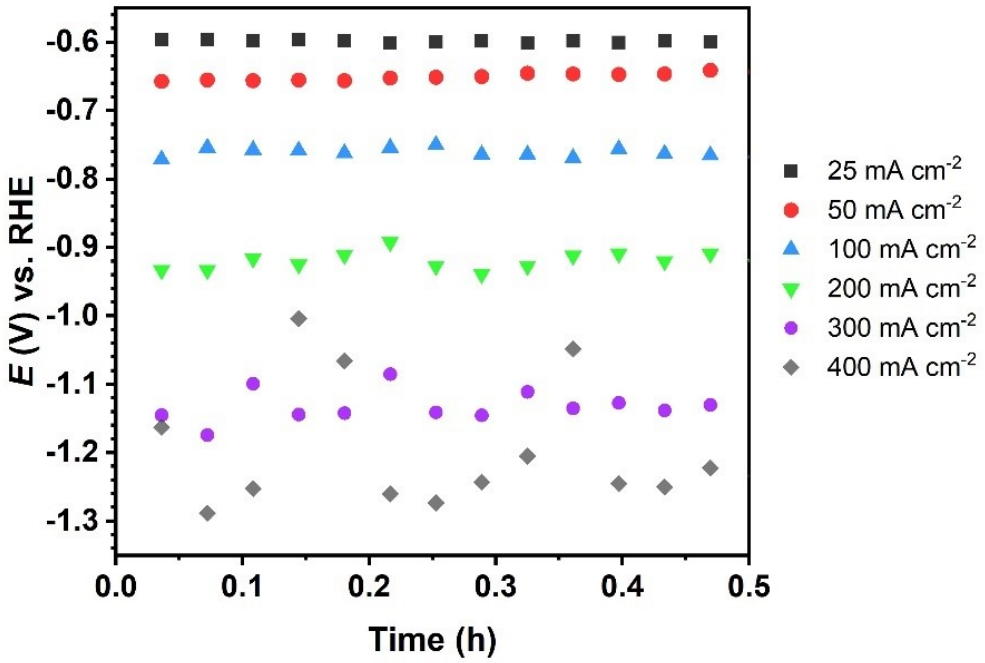

Figure S21. Chronopotentiometry measurements of **NiPc-B@CNT** in GDE with CO_2-saturated 1 M $KHCO_3$ electrolyte at different current densities (without *iR* correction).

The electrolytic potential fluctuated greatly only when the current reaches 400 mA cm^{-2} due to the bubbling issue.[3] We found that the electrolyte had penetrated the gas-liquid interface of GDE. Steady-state operation at higher current densities requires improved GDE devices.

Supporting Tables

Table S1. The relative energies (kcal mol^{-1}) for various conformations of **NiNc-B** and **NiNc-B@CNT**, as well as their binding energies (kcal mol^{-1}) calculated by xtb method.

C-M-N	**C-0-8**		**C-1-7**		**C-2-6**		**C-3-5**		**C-4-4**	**NiPc-B**
E_C	19.88		24.15		16.91		15.44		0	\
CMN	**C08**	**C80**	**C17**	**C71**	**C26**	**C62**	**C35**	**C53**	**C44**	\
$E_{C\text{-}CNT}$	0	59.04	0	63.29	56.80	50.99	49.12	47.86	52.58	\
E_b	-59.29	-0.25	-63.10	-0.27	0.48	-5.33	-5.73	-6.98	13.17	-56.93
E_{Rb}	\	\	\	\	\	\	\	\	-38.95	\

C-M-N: various steady conformations of **NiNc-B**;

CMN: binding models of **NiNc-B@CNT**;

E_C: Energy for various **NiNc-B** conformations;

$E_{C\text{-}CNT}$: Energy for various binding conformation of **NiNc-B** loaded on CNTs;

E_b: Binding energy, $E_b = E_{C\text{-}CNT} - E_C - E_{CNT}$;

E_{Rb}: Relative binding energy while $E_{C\text{-}CNT}$ is the energy of the most stable binding moles (**C08** or **C17**).

Table S2. EXAFS fits parameters.

Sample	Fit	Region	Shell,N	R, Å	E_0	ss.^{2} (10^{-3})	R-factor	Reduced Chi-square
NiNc-B	1	I	Ni.N,4	1.88	-6.9	3.1	0.0137	291
	2	I,II	Ni-N,4 Ni-C,8	1.89 2.91	-4.2	2.7 4.4	0.0132	113
	3	I,II,III	Ni-N,4 Ni-C,8 Ni-C,16	1.89(1) 2.93(2) 3.15(3)	-4.8 (2.4)	3.0 (0.8) 2.7 (1.4) 5.0 (3.2)	0.0101	67
NiPc-B	4	I	Ni.N,4	1.85	-9.8	3.7	0.0623	152
	5	I,II	Ni-N,4 Ni-C,8	1.86 2.88	-7.1	3.1 6.4	0.0232	80
	6	I,II,III	Ni-N,4 Ni-C,8 Ni-C,16	1.87(1) 2.89(2) 3.09(4)	-6.2 (2.4)	3.5 (0.8) 4.1 (1.6) 10.1 (7.6)	0.0099	26
NiPc-B@CNT	7	I	Ni-N, 4	1.89	-4.4	2.7	0.0103	288
	8	I,II	Ni.N,4 Ni-C,8	1.89 2.92	-4.3	2.2 4.2	0.0143	158
	9	I,II,III	Ni.N,4 Ni-C,8 Ni-C,16	1.91(1) 2.94(2) 3.11(4)	-1.1 (2.3)	2.5 (0.8) 2.1 (1.4) 11.5 (7.4)	0.0079	68
NiPc-B@CNT@CC (before catalysis)	10	I	Ni-N, 4	1.89	-5.6	3.7	0.0063	78
	11	I,II	Ni.N,4 Ni-C,8	1.89 2.92	-4.7	3.0 4.9	0.0131	64
	12	I,II,III	Ni.N,4 Ni-C,8 Ni-C,16	1.91 (1) 2.94 (1) 3.11 (4)	-2.0 (2.1)	3.4 (0.8) 2.4 (1.2) 11.2 (6.3)	0.0063	24
NiPc-B@CNT@CC (after catalysis)	13	I	Ni-N, 4	1.89	-5.4	3.2	0.0073	144
	14	I,II	Ni.N,4 Ni-C,8	1.89 2.92	-4.6	2.6 4.7	0.0128	101
	15	I,II,III	Ni.N,4 Ni-C,8 Ni-C,16	1.91(1) 2.94(1) 3.11(3)	-1.8 (2.1)	3.0 (0.8) 2.3 (1.2) 11.2 (6.5)	0.0067	41

* The amplitude reduction factor S_0^2 was fixed to 1. Region I refers to the EXAFS spectra region between apparent distances 1.2-2 Å, Regions I, II refer to that between 1.2 -2.7 Å and Regions I, II, III refer to that between 1.2-3.2 Å. We note that the data resolution, the ability to distinguish between 2 bond distances, given by $\pi/2\Delta k$ is ~ 0.14 Å. The **NiPc-B** complex upon deposition CNTs and CC, respectively, further illustrate small changes along the rising edge at 8341 and 8353 eV, indicating differences within the local coordination sphere upon anchorage. Accordingly, the results of **NiPc-B** show a slight elongation in the Ni-N and Ni-C distances of ~0.04 Å and ~0.02-0.05 Å upon deposition on CNTs and CC, respectively. The averaged Ni-N and Ni-C distances in **NiPc-B** are observed at 1.87 ± 0.01 Å, 2.89 ± 0.02 Å and 3.09 ± 0.04 Å (Table S2), whereas those in **NiPc-B@CNT** and **NiPc-B@CNT@CC** illustrate slightly elongated Ni-N and Ni-C distances at 1.91 ± 0.01 Å, 2.94 ± 0.02 Å and 3.11 ± 0.04 Å (Table S2).

Table S3. Summary of the bond distances of calculated Ni-based complexes. Bond distances are in Å.

Complexes	Ni-N_1	Ni-N_2	Ni-N_3	Ni-N_4
NiNc-B	1.93	1.93	1.93	1.93
NiPc-B	1.91	1.91	1.90	1.90

Table S4. Natural charges of the atoms 1-11 and atom Ni in **NiPc-B** and **NiNc-B** calculated by natural population analysis.

	Ni	N(8)	Σatom 1-9	O(10)	O(11)
NiNc-B	0.66	-0.54	0.67	-0.56	-0.56
NiPc-B	0.63	-0.54	0.19	-0.51	-0.51

Table S5. Performance summary of **NiPc-B@CNT** and the state-of-art electrocatalysts for CO_2RR with gas-diffusion electrode.

Catalyst	Electrolyte	*j* (mA cm^{-2})	FE_{CO}(%)	*E* (V) vs. RHE	Stability	TOF (s^{-1})	TON	Ref
NiPc-B@CNT	1 M $KHCO_3$	150	>99	-0.67[a]	18 h	13.77	892296	This work
		400	95	\	\	35.02	\	
CoPc/GDY/G	1 M $KHCO_3$	100	97	-0.82[b]	\	28	\	4
Fe^{3+}-N-C	0.5 M $KHCO_3$	50	90	-0.41[a]	28 h	0.14	14477	5
		104	90	-0.45[a]	\	0.3		
Fe-N-C	0.5 M KOH	55	40	\	20 h	0.513	36968	6
CoPc@Fe-N-C		90	>85	\	20 h	1.34	96258	
		296	93	-0.84[a]	\	4.82100	\	
CoPc2@MWCNTs	1 M KOH	116	96	-0.72[b]	3 h	2.7	29160	7
		75	94	-0.65[b]	10 h	1.67	60120	
		176	94	-0.92[b]	\	3.9	\	
Ni-CNC-1000	1 M KOH	100	<81.3	-0.9[b]	30 h	1.49	160872	8
Co^{II}QPyPhen	1 M $KHCO_3$	100	>99	-1.05 ~ -1.1[b]	8 h	19.59	564095	9
		116	100	-0.735[a]	\	22.95	\	
NiPc-OMe-MDE	1 M $KHCO_3$	150	99.6	-0.61[a]	40 h	12	1728000	3
		400	99.1	-0.69[a]	\	31.8	\	
Mg-C_3N_4	1 M $KHCO_3$	100	90	\	4.2 h	2.83	42840	10
		300	90	\	\	8.49	\	
CoPc+phenol	1 M KOH	50	90	\	8 h	0.06	1728	11
		200	88	\	\	0.23	\	
NiTAPc/CNT	1 M $KHCO_3$	150	99.8	\	10 h	13.26	477394	12
		500	94.6	\	\	41.9	\	
CoTMAPc@CNT	1 M KOH	31	94.5	-0.4[a]	15 h	1.63	87836	13
		239	95.6	-0.7[a]	\	12.68	\	
NiPPc/CNT	1 M $KHCO_3$	100	99.7	\	30 h	3.27	352818	14
		300	99.8	\	\	9.81	\	

a: with different proportion of *iR* compensation
b: without *iR* compensation
TOF and TON data comes from literature or calculated based on reported data (total current densities, Faradic efficiency of CO, CO current density, ICP-MS or ICP-OES data, etc.)
The values of this work were missing due to the limitation of our GDE set-up, as described in Figure S21.
Then there are some missing values in the Table S5 because they are not given in the quoted reference or cannot be calculated according to their existing data.

References

1. B. Ravel and M. Newville, *J. Synchrotron. Radiat.*, 2005, **12**, 537-541.
2. J. J. Rehr and R. C. Albers, *Rev. Mod. Phys*, 2000, **72**, 621-654.
3. X. Zhang, Y. Wang, M. Gu, M. Y. Wang, Z. S. Zhang, W. Y. Pan, Z. Jiang, H. Z. Zheng, M. Lucero, H. L. Wang, G. E. Sterbinsky, Q. Ma, Y. G. Wang, Z. X. Feng, J. Li, H. J. Dai and Y. Y. Liang, *Nat. Energy*, 2020, **5**, 684-692.
4. H. Gu, L. Zhong, G. Shi, J. Li, K. Yu, J. Li, S. Zhang, C. Zhu, S. Chen, C. Yang, Y. Kong, C. Chen, S. Li, J. Zhang and L. Zhang, *J. Am. Chem. Soc.*, 2021, **143**, 8679-8688.
5. J. Gu, C. S. Hsu, L. Bai, H. M. Chen and X. Hu, *Science*, 2019, **364**, 1091-1094.
6. L. Lin, H. Li, C. Yan, H. Li, R. Si, M. Li, J. Xiao, G. Wang and X. Bao, *Adv. Mater.*, 2019, **31**, e1903470.
7. M. Wang, K. Torbensen, D. Salvatore, S. Ren, D. Joulie, F. Dumoulin, D. Mendoza, B. Lassalle-Kaiser, U. Isci, C. P. Berlinguette and M. Robert, *Nat. Commun.*, 2019, **10**, 3602.
8. X. Cao, L. Zhao, B. Wulan, D. Tan, Q. Chen, J. Ma and J. Zhang, *Angew. Chem. Int. Ed.*, 2022, **61**, e202113918.
9. L. Sun, V. Reddu, S. Xi, C. Dai, Y. Sheng, T. Su, A. C. Fisher and X. Wang, *Adv. Energy Mater.*, 2022, **12** DOI: 10.1002/aenm.202202108, in press.
10. Q. Wang, K. Liu, J. Fu, C. Cai, H. Li, Y. Long, S. Chen, B. Liu, H. Li, W. Li, X. Qiu, N. Zhang, J. Hu, H. Pan and M. Liu, *Angew. Chem. Int. Ed.*, 2021, **60**, 25241-25245.
11. S. Ren, D. Joulie, D. Salvatore, K. Torbensen, M. Wang, M. Robert and C. P. Berlinguette, *Science*, 2019, **365**, 367-369.
12. K. Chen, M. Cao, Y. Lin, J. Fu, H. Liao, Y. Zhou, H. Li, X. Qiu, J. Hu, X. Zheng, M. Shakouri, Q. Xiao, Y. Hu, J. Li, J. Liu, E. Cortés and M. Liu, *Adv. Funct. Mater.*, 2021, **32**, 2111322.
13. J. J. Su, J. J. Zhang, J. C. Chen, Y. Song, L. B. Huang, M. H. Zhu, B. I. Yakobson, B. Z. Tang and R. Q. Ye, *Energy & Environ. Sci.*, 2021, **14**, 483-492.
14. K. J. Chen, M. Q. Cao, G. H. Ni, S. Y. Chen, H. X. Liao, L. Zhu, H. M. Li, J. W. Fu, J. H. Hu, E. Cortes and M. Liu, *Appl. Catal. B-Environ.*, 2022, **306**, 121093.